Emergence of the bifurcation structure of a Langmuir–Blodgett transfer model

2014 Nonlinearity 27 2711

(http://iopscience.iop.org/0951-7715/27/11/2711)

IOP Publishing | London Mathematical Society Nonlinearity

Nonlinearity **27** (2014) 2711–2734 doi:10.1088/0951-7715/27/11/2711

Emergence of the bifurcation structure of a Langmuir–Blodgett transfer model

Michael H Köpf[1] **and Uwe Thiele**[2,3]

[1] Département de Physique, École Normale Supérieure, CNRS, 24 rue Lhomond, 75005 Paris, France
[2] Institut für Theoretische Physik, Westfälische Wilhelms-Universität Münster, Wilhelm Klemm Str. 9, D-48149 Münster, Germany
[3] Center of Nonlinear Science (CeNoS), Westfälische Wilhelms Universität Münster, Corrensstr. 2, 48149 Münster, Germany

E-mail: u.thiele@uni-muenster.de and michael.koepf@ens.fr

Received 13 March 2014, revised 27 June 2014
Accepted for publication 9 September 2014
Published 7 October 2014

Recommended by B Eckhardt

Abstract

We explore the bifurcation structure of a modified Cahn–Hilliard equation that describes a system that may undergo a first-order phase transition and is kept permanently out of equilibrium by a lateral driving. This forms a simple model, e.g., for the deposition of stripe patterns of different phases of surfactant molecules through Langmuir–Blodgett transfer. Employing continuation techniques the bifurcation structure is numerically investigated using the non-dimensional transfer velocity as the main control parameter. It is found that the snaking structure of steady front states is intertwined with a large number of branches of time-periodic solutions that emerge from Hopf or period-doubling bifurcations and end in global bifurcations (sniper and homoclinic). Overall the bifurcation diagram has a harp-like appearance. This is complemented by a two-parameter study in non-dimensional transfer velocity and domain size (as a measure of the distance to the phase transition threshold) that elucidates through which local and global codimension 2 bifurcations the entire harp-like structure emerges.

Keywords: bifurcation diagrams, nonlinear partial differential equations, pattern formation
Mathematics Subject Classification: 35Q35, 65P30

S Online supplementary data available from stacks.iop.org/no/27/2711/mmedia

1. Introduction

Pattern formation that occurs at moving three-phase contact lines, e.g., where a liquid recedes or advances on a solid substrate under a gas atmosphere, poses significant challenges to both the experimentalist and the theoretician. A prominent example are deposition patterns, like a ring-shaped coffee stain [1], that result from a dynamic process that involves hydrodynamic flow of a solution or suspension, the dynamics of the contact line and evaporation of the solvent [2,3]. The problem is significantly enriched by a surface activity of the solute, i.e. by the presence of surfactants, as then Marangoni forces resulting from spatially inhomogeneous surface tensions are induced by concentration gradients [4]. Although the creation or avoidance of deposition patterns is of high practical relevance [2] and experiments show that a large number of systems produce a wide variety of patterns [3], the understanding and control of this entire class of pattern formation processes is not yet well developed. Here we discuss a reduced model for the deposition of line patterns of surfactant molecules on a plate that is withdrawn from a water-filled trough covered by a floating surfactant monolayer and numerically analyse its solution and bifurcation behaviour. This shall allow us to better understand how the emergence of deposition patterns in out-of-equilibrium situations is related to equilibrium phase transitions that occur in the same system when considered without driving.

A frequently used mathematical framework for problems where the evolution of a free surface of a film or shallow droplet on a substrate needs to be described is the long-wave (or lubrication) approximation [5]. Assuming that all relevant fields have small gradients parallel to the solid substrate the governing hydrodynamic transport equations and boundary conditions (BCs) are asymptotically reduced to a single (for single layers of simple liquids [5–8]) or coupled (for two or more layers of simple liquids, or various complex liquids [4, 9–11]) fourth-order, strongly nonlinear partial differential equations that describe the evolution of film thickness profile(s) and pertinent concentration field(s). Up to now only a few works investigate the deposition of regular one-dimensional line patterns with such long-wave models [12–15]—mainly through direct time simulations of the derived long-wave evolution equations. Although this allows one to determine parameter regions where line patterns may be deposited, the technique is less than ideal when it comes to understanding the onset of patterning: the time-simulation results support several hypotheses regarding the role of local and global bifurcations in the patterning process (see, in particular, section 3.4 of [14] and the concluding paragraph of [15]) but they provide at best an incomplete picture of the bifurcation structure, in particular as they are not able to reveal unstable solutions that might coexist with the stable solutions that correspond to the deposition. A deeper analysis is asked for, if one wants to clearly identify the involved bifurcation types and to understand the entire underlying bifurcation structure.

Here, we focus on the Langmuir–Blodgett transfer of an insoluble monolayer of surfactant from the surface of a water bath onto a plate that is drawn out of the bath as sketched in figure 1. If one uses a suitable amphiphilic molecule as surfactant at conditions sufficiently close to a first-order structural liquid–liquid phase transition (liquid-expanded (LE) to liquid-condensed (LC), see note[4]) then the intermolecular interaction with the solid plate may trigger a phase transition in parts of the surfactant layer due to an effect called substrate-mediated condensation [16]. On a plate that moves out of a bath, the partial condensation results in rather regular

[4] The first-order structural transition is between the LE phase and the LC phase of the surfactant layer. One speaks of a 'substrate-mediated condensation' if for a thick sub-layer of water the surfactant layer remains in the LE one-phase region while on a very thin water layer the presence of the solid substrate underneath lowers the free energy of the condensed state and thus effectively facilitates condensation [16]. The effect is well studied for the phospholipid DPPC (dipalmitoylphosphatidylcholine), but should in principle occur for any surfactant that exhibits such a first-order transition.

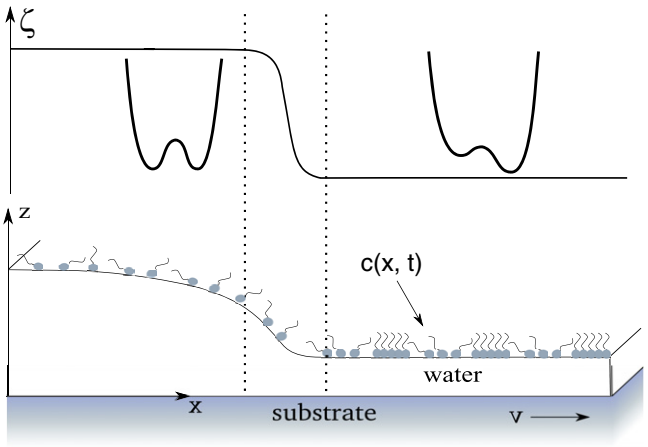

Figure 1. Sketch of the meniscus on a solid substrate during the transfer of a surfactant monolayer with velocity v. The surfactant density at the surface is denoted by $c(x,t)$. The function $\zeta(x)$ describes the change of the tilt of the free energy from the symmetric situation far away from the substrate (inset double well on the left) to the situation where the condensed state is energetically favoured (asymmetric double well on the right).

stripe patterns. They are preferentially oriented either parallel or perpendicular to the contact line. The wavelength of the resulting pattern depends on the plate velocity and temperature and can range from several micrometres down to a few hundred nanometres [17–19].

For this system there exists a full long-wave description in terms of coupled evolution equations for the film height profile and the concentration of an insoluble surfactant [12, 20] (that is a special case of a gradient dynamics description for such a coupled system [21]) as well as a reduced model in terms of a Cahn–Hilliard type evolution equation for a density with amendments to take substrate-mediated condensation into account [22]. Although the reduced model is a significantly simplified version of the full model, it captures all essential properties including the instabilities leading to stripe deposition parallel and perpendicular to the contact line and even reproduces the results of the full model in the case of structured substrates, where synchronization effects can be observed [23,24]. Most importantly, however, it allowed for a first analysis of the bifurcations related to the onset of pattern formation in the system. A preliminary bifurcation diagram has been obtained (see figure 2 below) by a combination of numerical path continuation of steady states that correspond to homogeneous deposition and direct numerical time simulation of time-periodic solutions that correspond to the experimentally observed deposition of regular line patterns.

It was found that a branch of stable time-periodic solutions exists for a range of plate velocities V. It ends at high V in a Hopf bifurcation (HB) and at low V in a homoclinic bifurcation. Furthermore, it was possible to reveal a structure of the bifurcation diagram in the range of low velocities which is best described by the term *front snaking* (see figure 2). The branch of steady solutions snakes back and forth, as more and more bumps are added (one per wiggle) to a localized structure in the transition region (i.e. front) between the bath surface and the drawn-out film. As a result, several (stable or unstable) steady solutions can exist at the same transfer velocity. This behaviour is reminiscent of homoclinic snaking, a phenomenon related to coexisting solutions with different numbers of localized structures that has been investigated in quite some detail for several pattern forming model equations like the standard Swift–Hohenberg equation [25–27] and the conserved Swift–Hohenberg equation [28] (often called phase-field crystal equation [29]). However, as further explained below, in our case, the

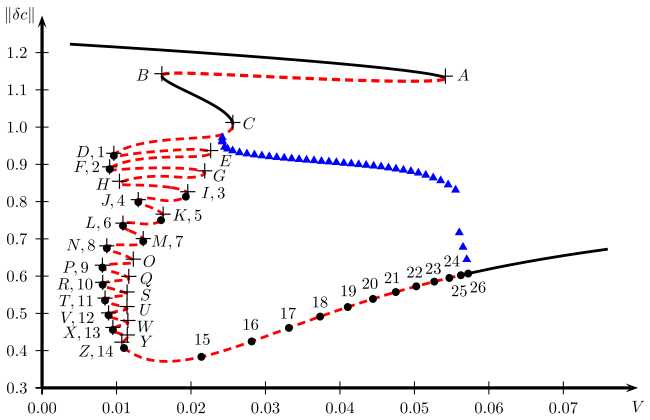

Figure 2. Shown is the (time-averaged) $\|\delta c\|$ (see equation (10)) norm of steady and time-periodic solutions of equation (3) in dependence of the dimensionless plate velocity V for $L = 100$, $\mu = 0.5$, $x_s = 10$, $l_s = 2$ and $c_0 = -0.9$. The solid and dashed lines represent stable and unstable steady states (homogeneous deposition), respectively, as obtained by numerical path continuation. The blue triangles correspond to time-periodic solutions (line deposition) obtained by direct numerical simulation. Letters A–Z label saddle-node bifurcations (folds), while numbers 1–26 label HBs. Selected steady profiles are given in figure 3. A movie relating the branch structure to the steady solution profiles $c(x)$ and the spectrum of their corresponding linear stability problem is available from the online supplementary material (stacks.iop.org/Non/27/2711/mmedia).

solutions on the snaking curve neither represent homoclinic nor heteroclinic orbits, but can be seen as different front states.

The numerical approach of [22] was limited w.r.t. the onset of patterning. It only permitted to find the loci of HBs on the branch of steady solutions, but could not be employed to determine the emerging branches of time-periodic solutions from start to end. Therefore, important questions regarding the onset of line pattern formation remain unanswered. The present work overcomes these limitations employing numerical continuation of stable and unstable branches of steady states (as in [22]) *and* of time-periodic solutions. The resulting completed bifurcation diagram in terms of our primary control parameter—the plate velocity V—is complemented by a study of its dependence on a second dimensionless control parameter that represents the ratio of the domain size to the typical patterning length, i.e. is inverse to the 'undercooling' or quench strength. The resulting two-parameter study allows us to start to understand through which codimension 2 local and global bifurcations the intertwined structure of snaking steady states and time-periodic solutions emerges.

The paper is structured as follows. Section 2 briefly reviews the geometric set-up and model equation of [22] that is employed here without change, followed by a presentation of the employed numerical method. Section 3 presents our results while section 4 concludes by discussing implications for systems that show similar transitions and by pointing out further open questions and challenges.

2. Model and numerical treatment

2.1. Evolution equation

The Langmuir–Blodgett transfer of surfactant monolayers close to a first-order phase transition of the surfactant layer can lead to regular stripe patterns. These stripes correspond to alternating

domains of different thermodynamic surfactant phases: the LE phase and the LC phase that can be seen as respective analogues of the gas phase and theliquid phase in a standard liquid–gas phase transition of a simple liquid. The dynamics of the stripe formation can be modelled through a long-wave approach that couples the sub-phase hydrodynamics to the non-equilibrium thermodynamics of the monolayer via the surfactant equation of state. Close to the first-order phase transition between the LE and LC phases, this equation can be determined through variation of a free energy of the prototypical Cahn–Hilliard double well type [30] and it describes how the surface tension of the liquid–air interface depends on the monolayer density, resulting in a Marangoni force and variations of the Laplace pressure [12,20,21]. An analysis of the results of [12] shows that the full long-wave model may be simplified [22] and the essential dynamics of the LE–LC domain formation through substrate-mediated condensation can be captured by an amended Cahn–Hilliard-type model. The resulting evolution equation consists of the generic Cahn–Hilliard equation describing the dynamics of phase decomposition [31] augmented by two additional terms: (i) a space-dependent external field to model the interaction between the monolayer and the substrate leading to the substrate-mediated condensation and (ii) a dragging term. The interaction between the monolayer and the substrate and thus the external field that represents it in the model change in the contact line region in a step-like manner. The drag term describes that the contact line region where the bath meets the moving plate recedes with nearly constant speed in the reference frame of the plate.

We focus on the situation where the contact line is straight and the plate is drawn in the direction orthogonal to the contact line. In this setting the evolution of the scalar field $c(x,t)$ that represents the concentration of surfactant on the surface of the liquid is captured by the non-dimensionalized evolution equation [22]

$$\partial_t c = \partial_x \left[\partial_x \frac{\delta F}{\delta c} - Vc \right], \tag{1}$$

where x is the spatial coordinate orthogonal to the contact line (see figure 1), t is time, and V is the speed at which the substrate is withdrawn. The substrate dependent interaction field that causes substrate-mediated condensation enters through an explicit space-dependent term $\zeta(x)$ in the free energy density

$$f(c,x) = \frac{1}{2}(\partial_x c)^2 - \frac{c^2}{2} + \frac{c^4}{4} + \mu\zeta(x)c. \tag{2}$$

It furthermore contains a gradient contribution that penalizes interfaces and a double-well potential. One may say that $\zeta(x)$ is responsible for a space-dependent tilt of the double-well potential.

The free energy density is integrated to obtain the total free energy $F = \int \mathrm{d}x f(c,x)$. We insert F into equation (1) and obtain the evolution equation

$$\partial_t c = -\partial_x^2 \left[\partial_x^2 c - c^3 + c - \mu\zeta(x) \right] - V\partial_x c. \tag{3}$$

Note that due to the space dependence of f, equation (3) is not invariant with respect to translations in x. Therefore one is not able to remove the advection term $V\partial_x c$ by a simple Galilei transform. With other words, the spatial dependence selects a particular frame of reference: the physical laboratory system.

The function ζ smoothly switches between two thermodynamically different regions: (i) left of the contact line ($x < x_s$, where x_s is the contact line position) the local free energy is a symmetric double-well potential, i.e. the LE and LC phases are energetically equivalent, and (ii) right of the contact line ($x > x_s$) the local free energy is tilted favouring the LC phase. For ζ we use the same hyperbolic tangent centred at $x = x_s$ as in [22]:

$$\zeta(x) = -\frac{1}{2}\left[1 + \tanh\left(\frac{x - x_s}{l_s} \right) \right]. \tag{4}$$

Thus, the constant l_s denotes the width of the transition region. For consistency with [22] we use the BCs

$$c(0) = c_0, \quad \partial_{xx}c(0) = \partial_x c(L) = \partial_{xx}c(L) = 0. \tag{5}$$

The density c_0 that is imposed at the inlet (left boundary, $x = 0$) of the system models the presence of a virtually non-depletable surfactant bath. In fact, in the experiments, the Langmuir trough is operated in a way that it keeps the surfactant surface pressure, and therefore the density, constant by displacing barriers at the surface of the trough. The influence of the conditions at the outlet (left boundary, $x = L$) on the pattern formation are discussed in section 4.

Finally we mention a number of related models. Krekhov [32], and Foard and Wagner [33, 34] use related Cahn–Hilliard-type models. In particular, they employ space-dependent free energies that are switched from single-well potentials to symmetric double-well potentials at a moving threshold, by switching the sign of the quadratic term of the free energy. Such a threshold models a quench front, dividing the spatial domain into a two-phase and a one-phase region. This differs from the situation considered here, as in our model the threshold divides two different two-phase regions, namely, the region near the boundary on the meniscus side where the free energy is a symmetric double well and the region where the double well is tilted. The state in the region with the symmetric double well is determined by the BC. The quench front investigated in [32–34] propagates into a one-phase region where the order parameter is spatially uniform. Thus, there is a simple relation between the front velocity and the flow of material to the quench front: if the value of the order parameter in this region is called $c^\star$, then the flow of material to the front is $c^\star V$ and remains constant with time. In contrast to this situation, the inflow of surfactant in our model is not constant but dynamically adjusts to keep the surfactant density at the left boundary constant. This reflects the physical reality of Langmuir–Blodgett transfer, where the surfactant influx is determined by the hydrodynamic flow field and the dynamics of the surfactant molecules at the water surface, which in turn are influenced by the Langmuir trough that keeps the surfactant density constant in the bath.

2.2. Non-dimensionalization

Although for consistency, we use throughout this article the non-dimensional equation (3) and non-dimensional parameter as in [22], to understand the physical role of the parameters it is instructive to review the underlying scaling. We indicate dimensional quantities by a tilde and write the dimensional equivalent of equation (3) as

$$\partial_{\tilde{t}}\tilde{c} = -M\partial_{\tilde{x}\tilde{x}}\left[\sigma\,\partial_{\tilde{x}\tilde{x}}\tilde{c} + \kappa(a\tilde{c} - \tilde{c}^3) - \tilde{\mu}\tilde{\zeta}(\tilde{x})\right] - \tilde{V}\partial_{\tilde{x}}\tilde{c}, \tag{6}$$

where M is a diffusional mobility, σ is related to interface tension, κ is an energy density scale, $\tilde{\mu}$ the chemical potential difference and $\tilde{V}$ is the plate velocity. Note that the concentration $\tilde{c}$ has no dimension as it is given as part per volume. The parameter a may be called a non-dimensional depth of quench into the two-phase region.

If one introduces the non-dimensional variables $c = \tilde{c}/\Gamma$, $t = \tilde{t}/\tau$ and $x = \tilde{x}/\ell$ with scales

$$\Gamma = a^{1/2}, \quad \tau = \frac{\sigma}{Ma^2\kappa^2} \quad \text{and} \quad \ell = \sqrt{\frac{\sigma}{a\kappa}} \tag{7}$$

for concentration, time and length, respectively, one obtains the dimensionless equation (3). In this way the model parameters are reduced to four: the non-dimensional chemical potential difference

$$\mu = \frac{\tilde{\mu}}{a^{3/2}\kappa}, \tag{8}$$

the non-dimensional plate velocity

$$V = \frac{\tau}{\ell}\,\tilde{V} = \frac{\sigma^{1/2}}{Ma^{3/2}\kappa^{3/2}}\,\tilde{V}, \tag{9}$$

the non-dimensional domain size $L = \tilde{L}/\ell$ and the scaled concentration at the meniscus-side boundary c_0. As the present study aims at understanding the onset of the deposition of line patterns observed in [22], the same scaling is used although other scalings exist that allow for distinct parametric studies within the same physical parameter space (see note [5]).

The main focus here is the dependence of the solution behaviour on the non-dimensional plate velocity that represents the primary control parameter. If one's main interest is in the influence of temperature (quench depth), as investigated in [18], the scaling sketched in the note[4] is more adequate. Here, the temperature-dependent parameter a that represents an 'undercooling' appears in all scales and dimensionless numbers (7)–(9).

The resulting bifurcation diagram in terms of our primary control parameter shall be complemented by a study of transitions triggered by changing a second parameter that represents a distance to the threshold of structure formation at equilibrium. In the given scaling, we chose the dimensionless domain size L, i.e. the ratio of the physical domain size $\tilde{L}$ to the typical patterning length ℓ. If one assumes the undercooling a and energy scale κ are fixed, changing L amounts to a change of the interface tension σ. We note, however, that it is difficult in any experimental realization to change σ without changing κ and a as well. Although, one could chose μ or c_0 as second parameter, we think that this does not allow for such a clear physical interpretation as does the choice of V and L as control parameters. The two-parameter study in V and L presented in section 3 elucidates how the intertwined structure of snaking steady states and time-periodic solutions emerges.

2.3. Numerical approach

For the numerical continuation [35–37] of steady and time-periodic solutions of equation (3) with BC (5), we employ spatial discretization onto an equidistant grid of n points of distance $\mathrm{d}x = L/(n+1)$ and approximate the PDE by n ordinary differential equations (ODEs), one for each grid point. The interval $[\mathrm{d}x : L]$ is represented by $n = 380$ inner grid points. We keep the same number of grid points for every L. The interval starts at $\mathrm{d}x$ rather than at 0 as the value at $x = 0$ is fixed by the first BC (see equation (5)). This spatial grid matches exactly the grid used for the direct numerical simulations in [22], where two grid points at each boundary account for the BCs, yielding a total of 384 points. We choose second-order finite differences to approximate spatial derivatives, that is, again exactly the same discretization scheme that has been used in the direct numerical simulations in [22]. Due to the simplicity of this scheme, the BCs of the problem can be easily implemented what would, for example, not be the case with spectral Chebychev methods.

As a result we obtain a dynamical system consisting of n ODEs. It describes the time evolution of the concentration values c_i at equidistant points x_i. We use the package auto07p [35, 38] to (i) perform pseudo-arc length continuation [39] of fixed points of the dynamical system that correspond to steady solution profiles $c_0(x)$ of the PDE; to (ii) detect saddle-node and HBs of the fixed points, and most importantly (iii) to continue stable *and* unstable time-periodic solutions of the dynamical system that correspond to time-periodic solutions of the PDE that represent the deposition of regular line patterns. Furthermore we track (iv) the loci of saddle-node and HBs in an appropriate two-parameter plane.

[5] For instance, choosing the scales $\Gamma = (\tilde{\mu}/\kappa)^{1/3}$, $\tau = \sigma/M\kappa^{2/3}\tilde{\mu}^{4/3}$, and $\ell = \sigma^{1/2}/\kappa^{1/6}\tilde{\mu}^{1/3}$ one obtains equation (7) with M, σ, $\tilde{\mu}$ and κ set to one and without the tildes. The non-dimensional plate velocity is still $V = \tilde{V}\tau/\ell$ and the four remaining non-dimensional parameters are V, a, L and c_0.

Note that the unstable time-periodic solutions are not accessible by direct numerical integration since the numerical treatment necessarily involves fluctuations. However, the structure of the bifurcation diagram can only be completely understood if the unstable solutions are included. Continuation has previously been employed for kinetic equations like equation (3) and recent examples include studies of depinning droplets in 1D [40] and 2D [41,42], of drawn menisci of simple liquids [43] and of finite-time singularities in film rupture [44]. A brief overview is given in section 4.2 of [37].

The solutions of the model equations are vectors in a high dimensional space. In order to visualize and further analyse the bifurcation behaviour of the system, we define as solution measure the norm

$$||\delta c|| = \left[\frac{1}{TL}\int_0^T\int_0^L c(x,t)^2\,\mathrm{d}x\,\mathrm{d}t\right]^{1/2}, \tag{10}$$

where L is the domain size and T the temporal period for the time-periodic solutions. For steady states and when investigating system trajectories, the time average $(1/T)\int \mathrm{d}t\ldots$ is omitted.

3. Results

3.1. Steady profiles

In our previous investigation [22] a combination of direct numerical simulation and numerical continuation of steady solutions was used to construct a preliminary bifurcation diagram with the plate velocity V as primary control parameter, as summarized in figure 2. The diagram includes a family consisting of stable and unstable steady states (solid black and dashed red lines, respectively), and a branch of stable time-periodic solutions (blue triangles) that seems discontinuous close to its end at large V. The parameters employed with equation (3) are $L = 100$, $\mu = 0.5$, $x_s = 10$, $l_s = 2$ and $c_0 = -0.9$. With the exception of L these values are kept throughout the present study. A linear stability analysis of the steady solutions provides the loci of 26 HBs that are numbered 1–26 in figure 2. The 26 saddle-node bifurcations (folds) of the snaking curve are labelled by letters A–Z. Note that the various saddle-node and Hopf bifurcations are not created by a few eigenvalues that repeatedly cross the imaginary axis. Instead, nearly all of the HBs that are situated on the steady-state branch left of the point of minimal norm (at $V_{\min} \approx 0.015$) in figure 2 are related to different pairs of complex conjugate eigenvalues that acquire a positive real part. All of them become stable again on the piece of steady-state branch right of $V_{\min}$, giving rise to more HBs. The steady profile is linearly stable for $V \gtrsim 0.06$ where the last HB occurs. Therefore our further study focuses on the velocity range $0 < V < 0.1$ where all the mentioned bifurcations occur. Selected steady states profiles are shown in figure 3 and a movie relating the profiles to the structure of the branch of steady solutions and the spectrum of the corresponding linear stability problem is available from the online supplementary material (Movie_1_SteadyProfilesSpectrum.mp4). The spectrum can be obtained by solving the eigenproblem of the linear operator $\mathcal{L}'_c = -\partial_x^4 + (3\hat{c}^2 - 1)\partial_x^2 + (12\hat{c}\partial_x\hat{c} - V)\partial_x + 6(\hat{c}\partial_x^2\hat{c} + (\partial_x\hat{c})^2)$, which is obtained by straightforward linearization of (1) around the spatially inhomogeneous steady solution $\hat{c}(x)$ [22]. We solve the eigenproblem numerically using MATLAB.

On the snaking structure one observes two basic scenarios for the relation of saddle-node and Hopf bifurcations: in scenario (i) first a negative real eigenvalue crosses zero at a saddle-node bifurcation rendering the corresponding eigenmode unstable, then the same eigenvalue becomes negative again at a second saddle-node bifurcation, briefly before forming a complex conjugate pair together with another negative real eigenvalue. The complex conjugate pair then

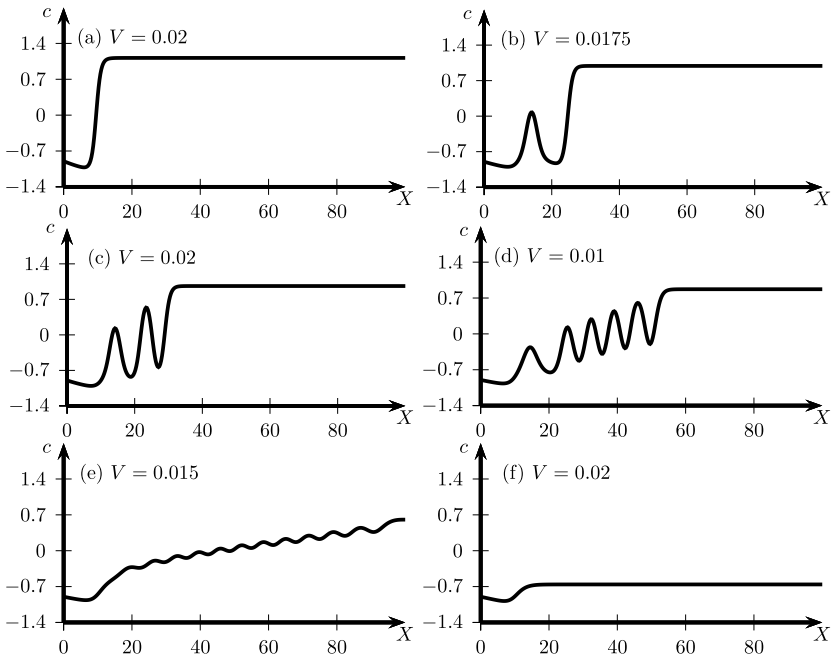

Figure 3. Examples of steady solution profiles from various points along the family of steady solutions in figure 2: (*a*) between the folds *B* and *C*, (*b*) between the folds *D* and *E*, (*c*) between the folds *G* and *H*, (*d*) between the folds *L* and *M*, (*e*) between the folds *Y* and *Z*, (*f*) to the right of HB 26. A movie relating the steady solution profiles $c(x)$ to the structure of the branch of steady solutions and the spectrum of their corresponding linear stability problem is available from the online supplementary material (stacks.iop.org/Non/27/2711/mmedia).

crosses the imaginary axis at a HB. Examples for this scenario are all such sequences from $(O, P, 9)$ to $(Y, Z, 14)$ in figure 2. As the second saddle-node and the Hopf bifurcation are often very close to each other the system might be very close to a codimension 2 Bogdanov–Takens bifurcation. In scenario (ii) first a complex conjugate pair of eigenvalues with negative real part crosses the imaginary axis at a HB. The pair then splits into two positive real eigenvalues. The smaller of the two becomes negative at a saddle-node bifurcation before it joins another negative real eigenvalue to become another complex conjugate pair of eigenvalues. Briefly afterwards the pair crosses the imaginary axis at a second HB. This second HB can form the first HB of the next such sequence. Examples for this scenario are all such sequences from $(3, J, 4)$ to $(7, N, 8)$ in figure 2.

Next, in section 3.2, we complete the bifurcation diagram for $L = 100$, by a systematic continuation of all branches of time-periodic solutions that emerge at the described HBs. Then, in section 3.3, we turn our attention to the snaking structure in the range $0.005 \lesssim V \lesssim 0.025$ of the bifurcation diagram. To better understand the relation of the saddle-node and Hopf bifurcations of the branch of steady solutions, we investigate how these structures and the time-periodic branches emerge/vanish when changing the dimensionless domain size L.

3.2. Completed bifurcation diagram for $L = 100$

To complete the bifurcation diagram figure 2, i.e. the case of $L = 100$ that is also investigated in [22], we continue all the branches of time-periodic solutions emerging at the HBs that we

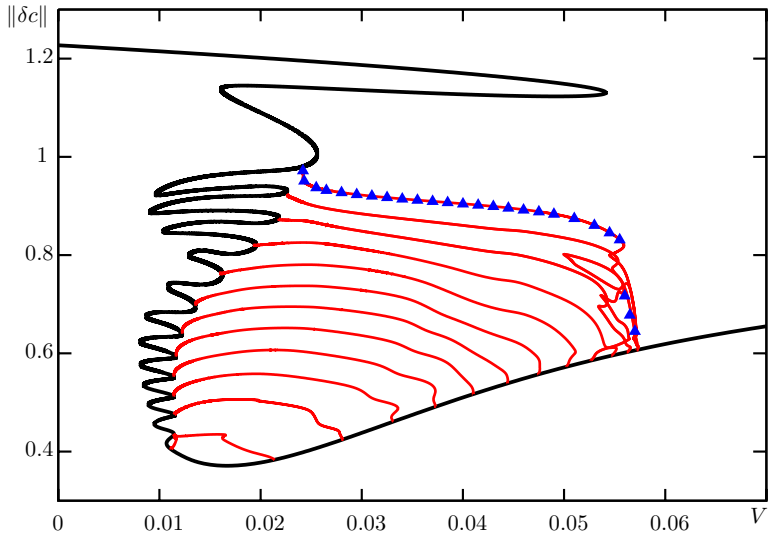

Figure 4. Shown is the (time-averaged) $|\delta c\|$ norm of steady and time-periodic solutions of equation (3) in dependence of the dimensionless plate velocity V for $L = 100$ and all the remaining parameters as in figure 2. The thick black solid and thin red solid lines represent steady states (homogeneous deposition) and time-periodic solutions (line deposition), respectively, as obtained by numerical path continuation. The blue triangles correspond to time-periodic solutions obtained by direct numerical simulation. Selected zooms showing important details are given in figures 5 and 6. Movies of time-periodic solutions on three different branches of periodic solutions at $V = 0.04$ are available as online supplementary material (stacks.iop.org/Non/27/2711/mmedia). Movies of time-periodic solutions on the two innermost branches of the harp-like structure are also available (stacks.iop.org/Non/27/2711/mmedia).

call 'primary Hopf branches', as well as selected branches of time-periodic solutions emerging from the primary Hopf branches in period-doubling bifurcations. The latter we call 'secondary Hopf branches'. As a result we find the harp-like structure presented in figure 4 with various close-ups shown in figures 5 and 6. Movies of time-periodic solutions on three different branches of periodic solutions at $V = 0.04$ are available as online supplementary material (stacks.iop.org/Non/27/2711/mmedia) as are movies of Time-periodic solutions on the two innermost branches of the harp-like structure (stacks.iop.org/Non/27/2711/mmedia). Each primary Hopf branch that starts either sub- or supercritically at HB 15 to HB 26, i.e. to the right of the point where the norm is minimal, eventually turns towards smaller V, continues to lower V ('spanning the harp') and finally ends in a global bifurcation on the snaking part of the branch of steady states. The global bifurcation is either a saddle-node infinite period (sniper) bifurcation or a homoclinic bifurcation [36, 45]. There are several secondary Hopf branches that connect a period-doubling bifurcation of a primary Hopf branch (e.g., solid red and dashed blue branches in figure 6) either to a global bifurcation on the snake (e.g., branch that connects the first PD of the HB 26 branch to a homoclinic bifurcation near fold C), or to a primary HB (e.g., branch that connects the second PD of HB 26 to HB 24, see figure 6(a)) or to another period-doubling bifurcation of a primary Hopf branch (not shown). Beside these extended branches, there are (very) short branches that emerge at HB 1 to HB 13 close to folds D, F, $I - N$, P, R, T, V, X and Z and connect to a global bifurcation nearby (beyond the next fold of the snaking structure). The following list summarizes the features of the five

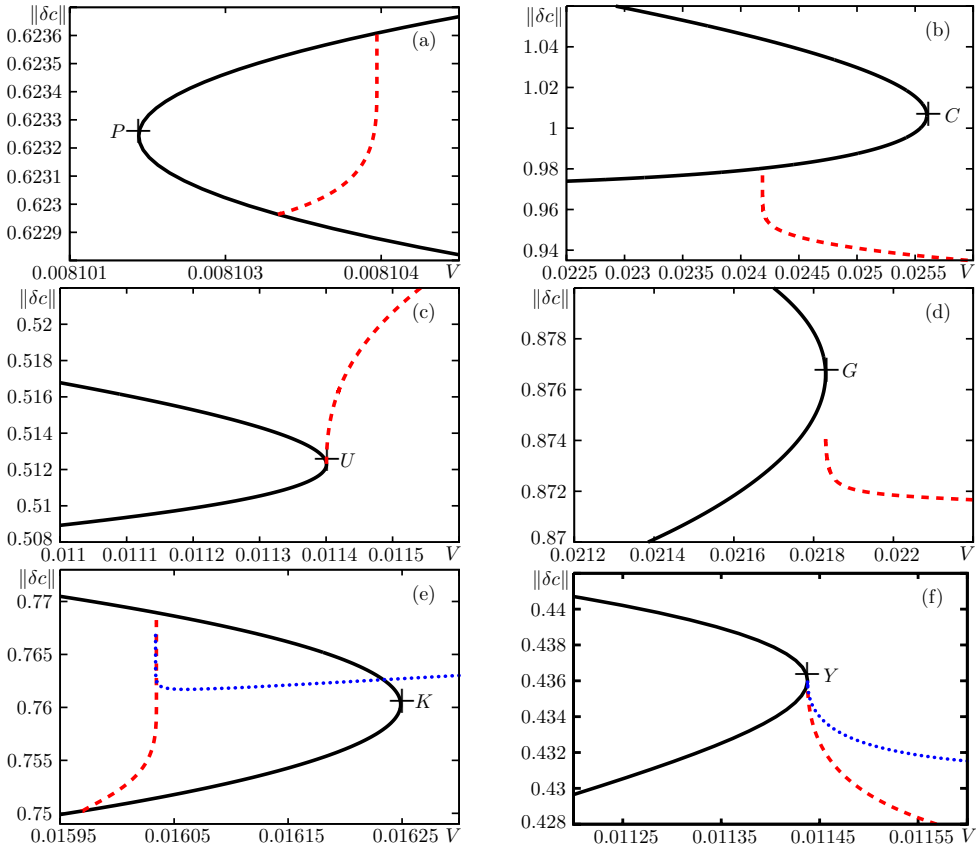

Figure 5. Close-ups of the bifurcation diagram figure 4 zooming in on qualitatively different endpoints of branches of time-periodic solutions that involve global bifurcations. Panels (*a*)–(*f*) correspond to cases (i1), (i2), (ii1), (ii2), (iii) and (iv) discussed in the main text.

different scenarios in which global bifurcations are observed at low V for branches that emerge from HBs or period-doubling bifurcations at higher V.

(i) The branch of time-periodic solutions monotonically approaches a vertical asymptote at some critical V and ends in a homoclinic bifurcation at an unstable steady state on the snake. One may distinguish sub-cases (i1) and (i2) with the branch of time-periodic states approaching the homoclinic bifurcation from the left and from the right, respectively. The case (i1) are the short branches emerging from HBs 1, 2, 4, 6 and 8–13 that lie completely within one bend of the snake. For an example see figure 5(*a*) (note the tiny V range). The case (i2) are the short branches emerging from HBs 3, 5 and 7 and the long branch that emerges from a period-doubling bifurcation of the HB 1 branch (see figure 5(*b*)). The latter branch consists mainly of the stable time-periodic solutions observed by direct time simulations [22].

(ii) The branch of time-periodic solutions monotonically approaches a vertical asymptote at a critical V that corresponds to a saddle-node bifurcation of the snake of steady states and ends in a sniper bifurcation. One may distinguish sub-cases (ii1) and (ii2) with the branch of time-periodic states approaching the saddle-node bifurcation from above in the

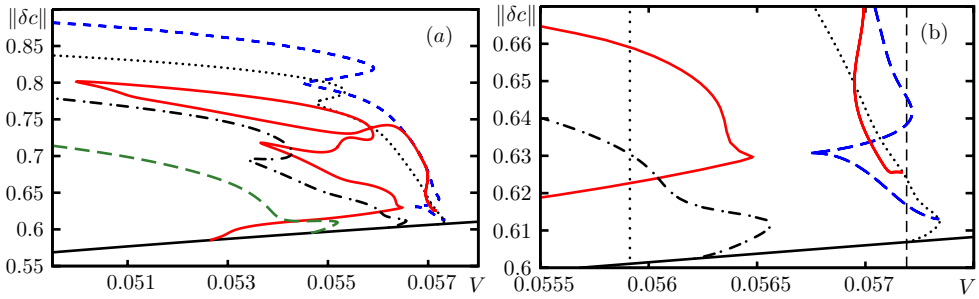

Figure 6. Close-ups of the bifurcation diagram figure 4 zooming in on period-doubling bifurcations and complex reconnections in the region $0.055 < V < 0.058$. Shown are all branches of periodic solutions that emerge from HB 26 (dotted), HB 25 (dotted–dashed), HB 24 (green long dashed), HB 23 (red solid line), as well as a secondary branch (blue short dashed) emerging from the first period-doubling bifurcation of the HB 26 branch. The stable time-periodic solutions observed in the direct time simulations lie on this secondary branch. Note that all the HBs at high velocities are subcritical. The vertical dashed line in panel (b) marks the velocity $V = 0.05719$ that is used for the time simulation shown in figure 7(a) and indicates the coexisting solutions at this velocity. The vertical dotted line at $V = 0.055\,913\,3$ in panel (b) indicates the velocity at which a transition from periodic to more complex dynamics is observed, as can be seen in figures 7(b) and (c).

$V - ||\delta c||$ plane and from below, respectively. The case (ii1) are the branches emerging from HBs 16–21. For an example see figure 5(c). The case (ii2) are the branches coming from HBs 15, 25 and 26 (see figure 5(d)).

(iii) Two branches of time-periodic solutions monotonically approach seemingly the same vertical asymptote at a critical V where they end in two homoclinic bifurcations. This occurs for the branches that emerge from HBs 3 and 24 and end at the branch between folds H and I as well as for the branches that emerge from HBs 5 and 22 and end at the branch between folds J and K (see figure 5(e). For our calculations the respective two homoclinic bifurcations occur at values of V that are identical up to four significant digits.

(iv) As (iii), but the two branches end in a sniper bifurcation at a fold (or in a sniper bifurcation and a homoclinic one very close nearby. This occurs for the branches that emerge from HBs 14 and 15 (see figure 5(f)). For our calculations the two bifurcations occur at values of V that are identical up to five significant digits. As we will explain later, this scenario is related to a codimension 2 bifurcation that creates the cases (i) and (ii).

The information regarding the branches of time-periodic solutions contained in figures 4– 6 goes well beyond [22] and sheds a new light on results obtained there. In particular, a weakly nonlinear analysis of the branch emerging at the HB at the highest velocity (HB 26) led to the conclusion that this HB is subcritical. However, in [22] it was also observed through time simulations, that the phase space trajectories of the system close to HB 26, where only one pair of complex conjugate modes becomes unstable, are very complicated: first, they exhibit a long phase of slow exponential growth (outwards spiral on a plane in phase space). After this initial phase, deviations from this planar dynamics are observed in the form of large excursions from the spiral which are then caught by a higher dimensional structure on which the trajectory eventually returns to the plane and begins to follow the spiral, again. This dynamics is not simply periodic and might be chaotic. An attempt to understand this behaviour as an example of a scenario described by Ovsyannikov and Shilnikov [46], which involves a stable and an

unstable pairs of complex conjugate eigenvalues failed because it was found that there is a strong interaction of the unstable mode and more than three of the stable modes [22].

In view of the close-ups of figure 4 in figure 6, the complicated trajectories and the higher dimensional structure which attracts the dynamics can be understood as a consequence of the existence of several (up to 12) stable and unstable time-periodic solutions at the same velocity value. The majority of these solutions is unstable. As the system spirals away from the unstable fixed point (steady-state solution) it feels the attracting and repelling presence of the various coexisting time-periodic solutions nearby. This can actually be seen in the results of direct numerical simulations performed at a value of V close to HB 26: once the initial amplification has become large enough, the system behaviour shows clear similarities to the time-periodic branches. This is indicated in figure 7 that shows phase plane representations of a simulated trajectory and of the various coexisting time-periodic branches at $V = 0.057\,19$. A corresponding movie is included in the online supplementary material (Movie_7_phaseplotV5719.mp4). One notes that although the trace of the simulated time evolution is similar to the time-periodic solutions, it does not approach any of them closely, indicating that they act as repellers. Even in very long simulations, the trajectory does not settle onto any of the stable time-periodic solutions, but eventually returns to a phase space region close to the unstable fixed point where the exponential amplification sets in again. However, the question whether this behaviour is persistent rather than transient remains open, as its persistence cannot be proven by direct numerical simulation. Nevertheless, we can estimate that a direct transition between periodic behaviour and more complicated, possibly chaotic behaviour occurs closely around $V_c \approx 0.055\,913\,3 \pm 10^{-7}$. At velocities $V < V_c$ the trajectory quickly settles on a limit cycle as is shown in figure 7(b) while we cannot identify a clear number of periods anymore for $V > V_c$ as can be seen in figure 7(c). The nature of this transition is yet unknown. Due to the sharpness of the transition a scenario involving a sequence of supercritical period doubling is unlikely and we conjecture that the new attractor for $V > V_c$ appears through a cascade of subcritical period doublings at larger velocities. However, at the moment we are not able to prove this with our numerical tools. Also, our estimate of V_c has to be taken with care: as one approaches V_c from below, the duration of a transient with seemingly simple periodic behaviour is longer and longer and it is therefore impossible to decide whether an orbit will stay periodic forever or finally become irregular. If the dynamics at $V > V_c$ was indeed chaotic, this would involve an infinite number of unstable periodic orbits. On the wildly undulated branch of periodic solutions that emerges from HB 23 and finally ends in the second period doubling on the branch that comes from HB 26, we find two torus bifurcations and two period doublings. Although switching branches at these points is beyond the capabilities of our current computational means, these findings indicate that the full picture in this region might be much more complicated than what is shown in figure 6. We conclude that based on our results we cannot rule out chaos. Note that the role of a large number of repellers in the transition to chaos has been analysed, e.g., in [47] for channel flow.

In the present section we have analysed the bifurcation structure for fixed $L = 100$ employing V as the main control parameter. To further understand how the observed harp-like structure emerges we next investigate how the bifurcation structure changes with our second control parameter L. Reduction of the system size will also lead to a deconvolution of the complicated branch structure shown in figure 6.

3.3. Simplification of bifurcation structure with decreasing domain size L

Up to here we have completed the bifurcation diagram figure 2, i.e. in the case of $L = 100$ partially given in [22], by a systematic continuation of the branches of time-periodic solutions

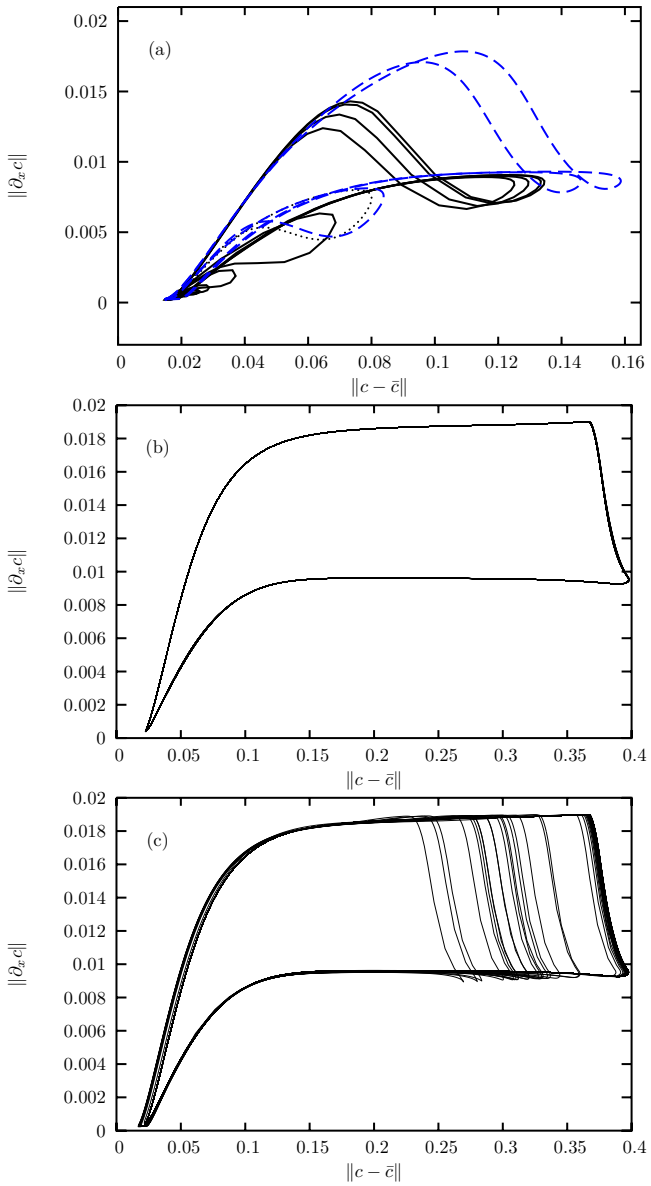

Figure 7. Shown are representations of various time-dependent solutions on the phase plane spanned by the norms of $c(x,t)-\bar{c}$ and of $\partial_x c(x,t)$, where $\bar{c}$ is the mean value of c. In (a) a trajectory obtained by direct numerical simulation at plate velocity $V = 0.05719$ (indicated by the vertical dashed line in figure 6(b)) is given as a thin solid line while the time-periodic branches obtained by numerical continuation are shown in the same line styles used in figure 6. A corresponding movie is included in the online supplementary material (Movie_7_phaseplotV5719.mp4). Panels (b) at $V = 0.055\,193\,2$ and (c) at $V = 0.0559134$ show that a direct transition between such complicated dynamics as in panel (a) and simple periodic behaviour is observed closely around the critical velocity $V_c \approx 0.055\,913\,3$ (indicated by the vertical dotted line in figure 6(b)).

emerging at all of the 26 HB. This has allowed for a classification of possible endings of branches of time-periodic solutions corresponding to the behaviour at the onset of line deposition. Overall, the analysis indicates that our particular system has a complicated bifurcation structure that involves saddle-node and Hopf bifurcations of steady states, period-doubling bifurcations of time-periodic solutions and various global bifurcations, namely sniper and homoclinic bifurcations.

These observations are in line with observations in the literature for a wider class of related systems that show deposition or depinning phenomena. For other line deposition phenomena, similar bifurcations are hypothesized based on time simulations in [13, 14]. In particular, [14] discusses in which way such line deposition patterns may be seen as resulting from depinning transitions, thereby relating the phenomena to the depinning of driven droplets on heterogeneous substrates [40, 42, 48, 49], rotating cylinders [50], or to the depinning of interface undulations from the advancing tip of an air finger in a liquid-filled channel [51,52]. In these related systems depinning can also occur through Hopf, sniper or homoclinic bifurcations. This will be further discussed in the conclusion.

The main physical ingredients of our particular system are a first-order phase transition and a lateral driving (towards the right-hand side, see figure 1) that keeps the system permanently out of equilibrium. Close to the left boundary (the meniscus side), the underlying energy is a symmetric double well. As the concentration on the boundary is fixed to a value close to one of the minima of the energy, the corresponding phase is preferred. This changes to the right of the critical position x_s where the double-well potential is tilted such that the other phase is preferred.

Considering our main influences, we already know that in the case without driving $V = 0$ one obtains a standard system that evolves towards equilibrium, i.e. in the right-hand part it approaches the high-concentration phase promoted by the tilted double well potential. Out of equilibrium one finds at low (large) V a homogeneous deposition of the preferred phase (the boundary phase). At intermediate V the interplay of driving and phase dynamics results in stripe deposition.

One can also expect that no structure formation will occur if the intrinsic length scale of the patterning ℓ is larger than the considered domain size $\tilde{L}$. This implies that the rich structure of the bifurcation diagram figure 4 should vanish step by step if $L = \tilde{L}/\ell$ is decreased. In the following, we focus on this stepwise simplification and, in order to observe it, we compute bifurcation diagrams for decreasing dimensionless domain size L that represents the ratio of dimensional domain size and intrinsic patterning length scale (see section 2.2). In the alternative scaling discussed in note[4], one would keep L fixed and reduce the quench depth a.

We focus on the range $50 \leqslant L \leqslant 100$ as for smaller L the distance x_s between the boundary and the position where the tilt of the potential part of the free energy changes becomes important and renders the emerging picture non-generic. Figure 8 shows the branch of steady solutions for various L in the considered range. A movie showing the change of the branch of steady states with the domain size continuously increasing from $L = 50$ to $L = 100$ is available from the supplementary material (Movie_8_SnakeL50L100.mp4). One notices that with increasing L, the snaking structure becomes larger, i.e. more and more pairs of saddle-node bifurcations emerge in subsequent hysteresis bifurcations, adding wiggles to the branch that then widen with increasing L. In this way, one passes from 12 folds at $L = 50$ to 26 folds at $L = 100$. This is of course expected, since with each turn of the snake, a bump is added to the solution profile until the part of the snake with the lowest norm corresponds to a state in which the complete domain to the right of the substrate-mediated condensation threshold is filled with bumps (see figure 3(*e*)). With increasing L, more bumps fit into the domain, thus prolonging the snake.

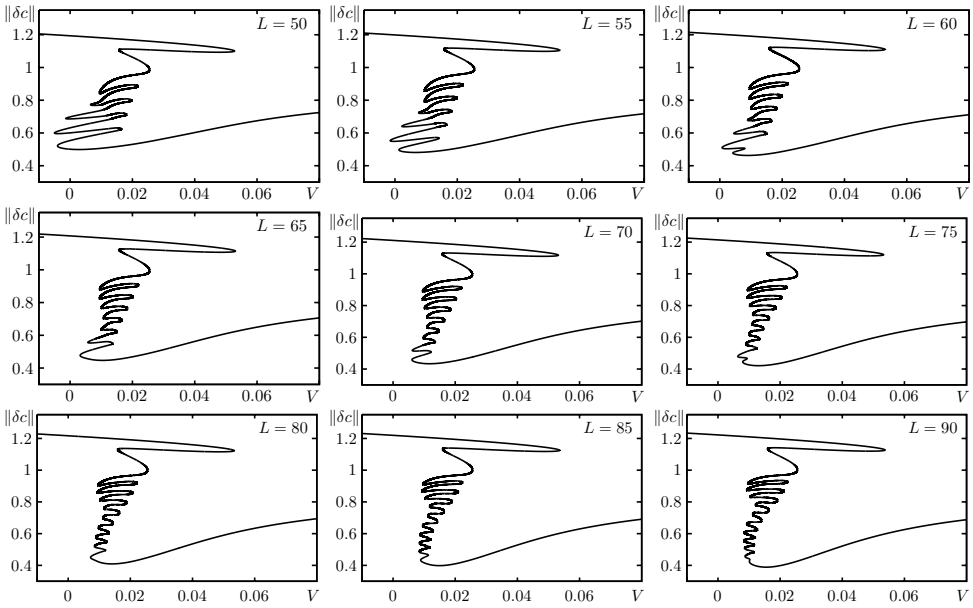

Figure 8. Shown is the branch of steady solutions for equally spaced values of the domain size from $L = 50$ to $L = 90$ as indicated in the individual panels. All the remaining parameters are as in figure 2. The occurring simplification with decreasing L is discussed in the main text. Figure 10 shows close-ups of the final bends of the snaking structure including the time-periodic branches for $L = 90$ to $L = 100$. A movie showing the change of the branch of steady states with the domain size continuously increasing from $L = 50$ to $L = 100$ is available from the online supplementary material (stacks.iop.org/Non/27/2711/mmedia).

However, from the continuation results shown in figure 4 one knows that the snaking structure is closely linked to the branches of time-periodic solutions. This raises the question what happens to the branches observed at $L = 100$ when the snaking structure shrinks with decreasing domain size L. Figure 9 shows the bifurcation diagram with steady and time-periodic solution for $L = 50$. One can see a smaller version of the harp-like structure that we observed for $L = 100$ in figure 4. Note in particular the simplified structure of the rightmost branches of periodic solutions as compared to the situation at $L = 100$ (see figure 6): the stable branch of periodic solutions now emerges directly from a HB, and not from period doubling. This implies that at some intermediate value of L, branch reconnections occur that result in the more complicated picture seen at $L = 100$.

With decreasing L, as more and more wiggles disappear from the branch of steady solutions, more and more branches of time-periodic solutions vanish as well and the structure shown in figure 4 evolves to the structure shown in figure 9.

We observe a generic sequence of transitions that eliminate branches of time-periodic solutions and the related global and local bifurcations in parallel to the elimination of folds of the snake when L is decreased. We explain the mechanism using the example of the time-periodic branches of lowest norm in figure 4, in particular the ones emerging from HBs 13–16. All the involved solution branches are shown for eight values of L between 92 and 100 in figure 10 while figure 11 shows the loci of the involved Hopf, homoclinic, sniper and saddle-node bifurcations in the parameter plane spanned by V and L.

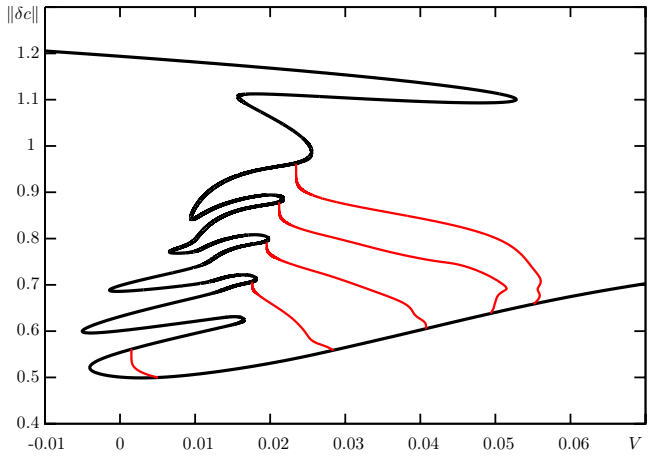

Figure 9. Shown is the (time-averaged) $\|\delta c\|$ norm of steady and time-periodic solutions of equation (3) in dependence of the dimensionless plate velocity V for $L = 50$ and all the remaining parameters as in figure 2. The thick black solid and thin red solid lines represent steady states (homogeneous deposition) and time-periodic solutions (line deposition), respectively, as obtained by numerical path continuation. Note, that the reconnection of the rightmost branches that is observed in the case $L = 100$ (see figure 4) is not observed at $L = 50$.

We describe the transitions with increasing L, i.e. the various bifurcations and branches are *created* subsequently. At $L = 90$ none of the HBs 13–16 and none of the related time-periodic branches exist, the lowest pair of saddle-node bifurcations of steady states has just been created in a hysteresis bifurcation at $L \approx 89.5$ (lower black solid line in figure 11). Slightly below $L = 91$ one observes a codimension 2 bifurcation that occurs close to the minimum of the curve of steady states. As a result a pair of HBs (HBs 13 and 16) appears together with the branch of time-periodic solutions that connects them. The creation of two HB corresponds to the minimum of the lower red dashed curve in figure 11 that indicates the loci of the two HBs. With increasing L, the two HBs move apart and the left (lower V) HB moves towards the lowest fold of the snake; see the bifurcation diagram at $L = 92$ in figure 10(h). At about $L = 92.5$, the branch of time-periodic solutions that connects HBs 13 and 16 breaks up into two disconnected branches. This happens when the branch of time-periodic solutions develops a protrusion that eventually collides with the unstable steady state slightly beside or directly at the lowest right fold (W). This codimension 2 bifurcation is marked by the lower blue filled circle in figure 11. The bifurcation diagram in figure 10(g) is at a slightly larger L, the two global bifurcations are already separated. The new left branch of time-periodic solutions coming from HB 13 at lower V now ends in a homoclinic bifurcation that moves towards smaller V (dotted line in figure 11) while the right branch of time-periodic solutions, coming from HB 16 at larger V, terminates in a sniper bifurcation at fold W. Further increasing L, the left branch becomes shorter and shorter, and practically disappears into fold X, while the right branch becomes longer as HB 16 moves continuously towards larger velocities and the other end remains at fold W (see figures 10(a)–(f) and figure 11). In the course of this process, there are also two folds created on the branch of time-periodic solutions that are again annihilated at about $L = 95$. Note that the HB and the homoclinic bifurcation that remain very close to the left fold (on opposite sites of it) could, in principle annihilate (and be recreated) in Bogdanov–Takens bifurcations [36, section 8.4.], but based on our limited numerical accuracy

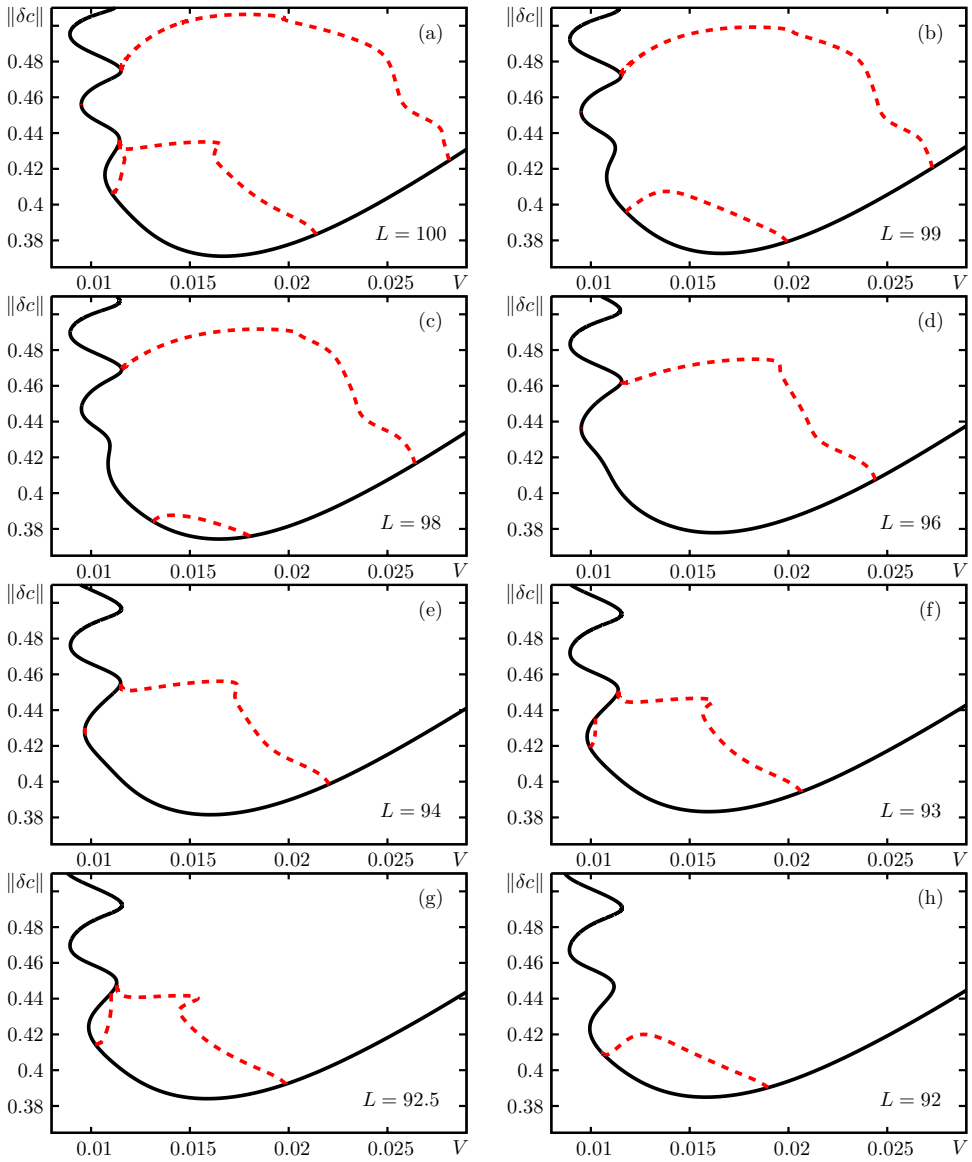

Figure 10. Shown are close-ups of the lower part of the snaking structure for various values of domain size L from 100 to 90 as indicated in the individual panels (*a*)–(*h*). The thick black solid and red dashed lines represent steady states (homogeneous deposition) and time-periodic solutions (line deposition), respectively, as obtained by numerical path continuation. Movies of time-periodic solutions on the lowest two branches in panel (*a*) are available from the online supplementary material (stacks.iop.org/Non/27/2711/mmedia).

we are not able to decide whether this actually happens between $L \approx 95$ and $L \approx 98$, at the locations marked by the red squares in figure 11.

Then the entire process is repeated: at about $L = 97.5$, a pair of saddle-node bifurcations of steady states is created (upper black solid line in figure 11) and a pair of HBs (HBs 14 and 15)

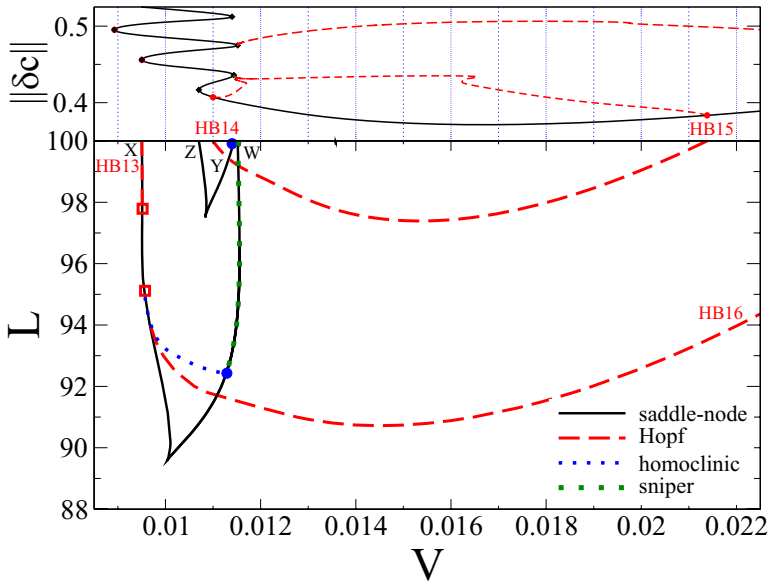

Figure 11. Loci of the folds W to Z (black solid lines), the HBs 13–16 (red dashed lines), and of the homoclinic bifurcation where the primary branch ends that emerges from HB 14 (dotted line). The labels of the HBs and folds correspond to the labels used in the $L = 100$ case in figure 2. Blue filled circles indicate where a branch of time-periodic solutions collides with the branch of steady states creating a homoclinic and a sniper bifurcation. Above the filled circle a sniper bifurcation coincides with the black solid line of the respective fold. The red squares indicate potential Bogdanov–Takens points where a homoclinic and a Hopf bifurcation emerge/annihilate, although no conclusive results could be obtained for HB 13 between $L = 95$ and $L = 98$.

appears together with the branch of time-periodic solutions that connects them (minimum of the upper red dashed line in figure 11). The two HBs move apart and the left one approaches fold Z, and two global bifurcations are created when the branch of time-periodic solutions connects to the steady-state branch close to fold Y (see the bifurcation diagrams in figures 10(a)–(c). By this mechanisms, new turns of the snake and new branches of time-periodic solutions can be generated for arbitrary system sizes.

4. Discussion and conclusion

We have explored the bifurcation structure of a modified Cahn–Hilliard equation that describes a system that may undergo a first-order phase transition and is kept permanently out of equilibrium by a lateral driving. The equation represents a reduced model that captures the main features of the stripe pattern formation observed before with a hydrodynamic long-wave description of Langmuir–Blodgett transfer with substrate-mediated condensation [12]. The modified Cahn–Hilliard model captures the main physical ingredients that are the first-order phase transition and the lateral driving that together with the pinning boundary condition on the meniscus side keeps the system permanently out of equilibrium. The system is biased towards one of the two phases only beyond a threshold position that represents the position of the contact line region in the physical system. The state in the boundary region on the meniscus side is determined by the boundary condition. In the literature other forms of such Cahn–Hilliard-type models are studied [32–34]. In particular, in these works a front that switches

the system between a stable one-phase and an unstable two-phase region of the phase diagram is moved through a fixed domain of given mean concentration. However, the onset of pattern deposition is not studied in a way that could be directly compared to our results. In particular, no bifurcations between steady states and time-periodic states (in the frame moving with the imposed front speed) are discussed.

Our analysis has shown that the snaking of steady states (observed in [22]) that correspond to various fronts between a homogeneous low concentration region close to the left domain boundary and a homogeneous state far away from the bath is intertwined with a large number of branches of time-periodic solutions that emerge from Hopf bifurcations or period-doubling bifurcations and end mainly in global bifurcations (sniper and homoclinic) but sometimes also in other period-doubling or Hopf bifurcations. Overall the various branches form a harp-like structure (see figure 4).

Beside the particular study of the bifurcation diagram for a fixed value of the domain size we have analysed how the bifurcation structure simplifies if one decreases the dimensionless domain size, i.e. increases the typical intrinsic length scale of pattern formation related to the first-order transition. We have shown that for decreasing L the rich bifurcation structure vanishes step by step through a number of codimension 2 bifurcations, namely, annihilation of pairs of homoclinic and sniper bifurcations, annihilations of pairs of period-doubling bifurcations, and annihilations of pairs of Hopf bifurcations. Beside these transitions involving branches of time-periodic solutions, the front snaking structure of steady solutions reduces by annihilations of pairs of saddle-node bifurcations.

The intriguing question of how the complicated bifurcation scenario at large domain size emerges is not only relevant for the system of Langmuir–Blodgett transfer but for a wider class of systems showing deposition and depinning phenomena. It has been argued in [14] that the onset of line deposition, i.e. the emergence of branches of time-periodic solutions may be seen as resulting from a depinning transition: when a homogeneous layer is deposited on the moving plate the concentration profile is steady in the laboratory frame and one may say that the concentration profile is pinned. However, when lines are deposited, in the laboratory frame they move away from the bath, i.e. the lines are depinned from the meniscus. This implies that one should not only expect to find similarities between the present study and other studies of the bifurcation structure behind deposition patterns as, e.g., [13–15] (see also review [3]), but see such similarities as well in studies of driven droplets depinning from substrate heterogeneities [40, 42, 48, 49] and rotating cylinders [50]; studies of driven clusters of interacting colloidal particles depinning in heterogeneous pores [53]; or studies of bubbles advancing in a channel with a central geometrical constraint, where the bubbles develop undulations that are steady in the laboratory frame [51, 52]. In the frame moving with the uniformly advancing tip of the bubble the undulations depin from the tip similar to the depinning of a deposition pattern from the contact line region. A related effect is also observed in abrasive water-jet cutting, a technique of cutting material with a focused beam of abrasive particles accelerated by water that is moved across the material [54, 55]. There is a model based on a Kuramoto–Sivashinsky-type equation that shows a transition from smooth cuts (analogous to our homogeneous deposition) to ripples and striations patterns (analogous to our line deposition) [56, 57]. In this system the undulations represent structures that depin from the moving cutting jet.

In all these systems the transition from steady (pinned) states to time-periodic (depinned) states is also found to occur through sub- or supercritical Hopf, sniper or homoclinic bifurcations. Although transitions between different scenarios where observed, in particular, in [14,40,42,48], the occurring codimension 2 bifurcations involving time-periodic states have not yet been identified.

For each of the mentioned systems one can find a physically meaningful control parameter whose variation brings the system into a part of the parameter space where no large amplitude structures exist, i.e. the system becomes either steady at all values of the imposed driving (here the plate velocity V) or only allows for small-amplitude 'surface waves' (as in the Kuramoto–Sivashinsky limit of the convective Cahn–Hilliard or thin film equation). However, although depinning and deposition patterns are widely occurring, to our knowledge no systematic study exists for any of the mentioned systems that investigates the emergence/vanishing of the rich bifurcation structure related to depinning or pattern deposition that should characterize these systems. Therefore, the results obtained here will be of some relevance to other similar systems as they provide a sound basis for comparison.

The present study is limited in two important ways. On the one hand, it is a study of solutions to a partial differential equation with one spatial dimension only, i.e. the described involved bifurcation structure only captures solutions that are invariant w.r.t. translations along the contact line and is, e.g., not able to capture the transition between the deposition of stripes parallel and perpendicular to the contact line observed in [12, 22, 23] for Langmuir–Blodgett transfer and in the Cahn–Hilliard-type models where quench fronts are moved through the system [32, 34]. Further large-scale numerical bifurcation studies will be needed to systematically explore the full solution space for out-of-equilibrium amended Cahn–Hilliard-type models allowing for a breaking of the transversal translational symmetry in analogy to such studies for depinning droplets [42, 58]. However, also the latter need to be extended to understand how the entire bifurcation structure vanishes if one goes from partially wetting liquids to completely wetting liquids.

We remark that a future study should also further investigate the influence of the boundary conditions, in particular, on the meniscus side. The need of boundary conditions that allow for a controlled through-flow of material as in the present system is a common complication in dragged plate problems. In the case of simple liquids, recently a central manifold reduction was employed to rigorously derive an asymptotic series for the meniscus side that can then be used to construct boundary conditions that do not introduce an additional domain-size dependence [59]. Such an approach has still to be developed for complex fluids. The boundary conditions at the outlet do not influence the formation of domains at the meniscus, as long as the system is large enough—for the used parameters $L \gtrsim 50$. However, the structure of the snake is intimately related to the system's finite extent as its lower end is reached when the whole domain is filled by periodic structures (see figure 3). It would be of great theoretical interest to understand the transition to a spatially infinite system where the high velocity end of the patterning range can be conjectured to correspond to a transition from absolute to convective instability. This idea is substantiated by a previous calculation that predicts the velocity corresponding to the final Hopf bifurcation by determination of a front velocity through a marginal stability analysis [22].

On the other hand, the present study is entirely based on numerical path continuation while the analytical results obtained in [22] are entirely based on linear and weakly nonlinear analyses. As it is not to be expected that the uncovered complex bifurcation scenario of the full PDE can be treated analytically, there is a strong need for further simplified models based on ordinary differential equations (ODE) that are able to reproduce the main features described here. We expect that they need to be at least four-dimensional. Note, that the authors of [42] were able to use selected results of the ODE studies in [60, 61] to explain certain aspects of the depinning behaviour of droplets, however, also there the 'mapping' remains rather incomplete. We hope that our numerical studies of the bifurcation structure of deposition and depinning processes can motivate the development of generic ODE models for this class of processes.

Acknowledgments

The authors are grateful to the Newton Institute in Cambridge, UK, for its hospitality during their stay at the programme 'Mathematical Modelling and Analysis of Complex Fluids and Active Media in Evolving Domains' where part of this work was done. MHK acknowledges the support by the Human Frontier Science Program (Grant RGP0052/2009-C). This publication is based in part on work supported by Award No KUK-C1-013-04, made by the King Abdullah University of Science and Technology (KAUST), and LabEX ENS-ICFP: ANR-10-LABX-0010/ANR-10-IDEX-0001-02 PSL*.

References

[1] Deegan R D 2000 Pattern formation in drying drop *Phys. Rev.* E **61** 475–85
[2] Han W and Lin Z 2012 Learning from 'Coffee Rings': ordered structures enabled by controlled evaporative self-assembly *Angew. Chem. Int. Ed.* **51** 1534–46
[3] Thiele U 2013 Patterned deposition at moving contact line *Adv. Colloid Interface Sci.* **206** 399–413
[4] Craster R V and Matar O K 2009 Dynamics and stability of thin liquid film *Rev. Mod. Phys.* **81** 1131–98
[5] Oron A, Davis S H and Bankoff S G 1997 Long-scale evolution of thin liquid film *Rev. Mod. Phys.* **69** 931–80
[6] Mitlin V S 1993 Dewetting of solid surface: analogy with spinodal decomposition *J. Colloid Interface Sci.* **156** 491–7
[7] Sharma A and Khanna R 1998 Pattern formation in unstable thin liquid film *Phys. Rev. Lett.* **81** 3463–6
[8] Thiele U 2010 Thin film evolution equations from (evaporating) dewetting liquid layers to epitaxial growth *J. Phys.: Condens. Matter* **22** 084019
[9] Pototsky A, Bestehorn M, Merkt D and Thiele U 2005 Morphology changes in the evolution of liquid two-layer films *J. Chem. Phys.* **122** 224711
[10] Náraigh L Ó and Thiffeault J L 2010 Nonlinear dynamics of phase separation in thin films *Nonlinearity* **23** 1559–83
[11] Thiele U, Todorova D V and Lopez H 2013 Gradient dynamics description for films of mixtures and suspensions: dewetting triggered by coupled film height and concentration fluctuations *Phys. Rev. Lett.* **111** 117801
[12] Köpf M H, Gurevich S V, Friedrich R and Chi L 2010 Pattern formation in monolayer transfer systems with substrate-mediated condensation *Langmuir* **26** 10444–7
[13] Frastia L, Archer A J and Thiele U 2011 Dynamical model for the formation of patterned deposits at receding contact lines *Phys. Rev. Lett.* **106** 077801
[14] Frastia L, Archer A J and Thiele U 2012 Modelling the formation of structured deposits at receding contact lines of evaporating solutions and suspensions *Soft Matter* **8** 11363–86
[15] Doumenc F and Guerrier B 2013 Self-patterning induced by a solutal Marangoni effect in a receding drying meniscus *Europhys. Lett.* **103** 14001
[16] Riegler H and Spratte K 1992 Structural changes in lipid monolayers during the langmuir-blodgett transfer due to substrate/monolayer interactions *Thin Solid Films* **210–211** (Part 1) 9–12
[17] Gleiche M, Chi L F and Fuchs H 2000 Nanoscopic channel lattices with controlled anisotropic wetting *Nature* **403** 173–5
[18] Köpf M H, Harder H, Reiche J and Santer S 2011 Impact of temperature on the LB patterning of DPPC on mica *Langmuir* **27** 12354–60
[19] Li L, Köpf M H, Gurevich S V, Friedrich R and Chi L 2012 Structure formation by dynamic self-assembly *Small* **8** 488–503
[20] Köpf M H, Gurevich S V and Friedrich R 2009 Thin film dynamics with surfactant phase transition *Europhys. Lett.* **86** 66003
[21] Thiele U, Archer A J and Plapp M 2012 Thermodynamically consistent description of the hydrodynamics of free surfaces covered by insoluble surfactants of high concentration *Phys. Fluids* **24** 102107
[22] Köpf M H, Gurevich S V, Friedrich R and Thiele U 2012 Substrate-mediated pattern formation in monolayer transfer: a reduced model *New J. Phys.* **14** 023016
[23] Köpf M H, Gurevich S V and Friedrich R 2011 Controlled nanochannel lattice formation utilizing prepatterned substrates *Phys. Rev.* E **83** 016212
[24] Wilczek M and Gurevich S V 2013 Synchronization in Cahn-Hilliard models for Langmuir–Blodgett transfer *ArXiv e-prints* arXiv:1308.6691

[25] Burke J and Knobloch E 2006 Localized states in the generalized Swift-Hohenberg equation *Phys. Rev.* E **73** 056211
[26] Burke J and Knobloch E 2007 Homoclinic snaking: structure and stability *Chaos* **17** 037102
[27] Knobloch E 2008 Spatially localized structures in dissipative systems: open problems *Nonlinearity* **21** T45–60
[28] Thiele U, Archer A J, Robbins M J, Gomez H and Knobloch E 2013 Localized states in the conserved Swift-Hohenberg equation with cubic nonlinearity *Phys. Rev.* E **87** 042915
[29] Emmerich H, Löwen H, Wittkowski R, Gruhn T, Tóth G I, Tegze G and Gránásy L 2012 Phase-field-crystal models for condensed matter dynamics on atomic length and diffusive time scales: an overview *Adv. Physics* **61** 665–743
[30] Cahn J W and Hilliard J E 1958 Free energy of a nonuniform system. 1. Interfacial free energy *J. Chem. Phys.* **28** 258–67
[31] Cahn J W 1965 Phase separation by spinodal decomposition in isotropic system *J. Chem. Phys.* **42** 93–9
[32] Krekhov A 2009 Formation of regular structures in the process of phase separation *Phys. Rev.* E **79** 035302
[33] Foard E M and Wagner A J 2009 Enslaved phase-separation fronts in one-dimensional binary mixture *Phys. Rev.* E **79** 056710
[34] Foard E M and Wagner A J 2012 Survey of morphologies formed in the wake of an enslaved phase-separation front in two dimensions *Phys. Rev.* E **85** 011501
[35] Doedel E, Keller H B and Kernevez J P 1991 Numerical analysis and control of bifurcation problems (I) Bifurcation in finite dimensions *Int. J. Bifurcation Chaos* **1** 493–520
[36] Kuznetsov Y A 2010 *Elements of Applied Bifurcation Theory* 3rd edn (New York: Springer)
[37] Dijkstra H A *et al* 2014 Numerical bifurcation methods and their application to fluid dynamics: Analysis beyond simulation *Commun. Comput. Phys.* **15** 1–45
[38] Doedel E J and Oldeman B E 2009 *AUTO07p: Continuation and bifurcation software for ordinary differential equations* (Montreal, Concordia University)
[39] Keller H B 1977 *Numerical Solution of Bifurcation and Nonlinear Eigenvalue Problems* (New York: Academic) pp 359–84
[40] Thiele U and Knobloch E 2006 On the depinning of a driven drop on a heterogeneous substrate *New J. Phys.* **8** 313
[41] Beltrame P and Thiele U 2010 Time integration and steady-state continuation method for lubrication equations *SIAM J. Appl. Dyn. Syst.* **9** 484–518
[42] Beltrame P, Knobloch E, Hänggi P and Thiele U 2011 Rayleigh and depinning instabilities of forced liquid ridges on heterogeneous substrates *Phys. Rev.* E **83** 016305
[43] Galvagno M, Tseluiko D, Lopez H and Thiele U 2014 Continuous and discontinuous dy- namic unbinding transitions in drawn film flow *Phys. Rev. Lett.* **112** 137803
[44] Tseluiko D, Baxter J and Thiele U 2013 A homotopy continuation approach for analysing finite-time singularities in thin liquid films *IMA J. Appl. Math.* **78** 762–76
[45] Strogatz S H 1994 *Nonlinear Dynamics and Chaos* (Addison-Wesley)
[46] Ovsyannikov I M and Shil'nikov L P 1992 Systems with a homoclinic curve of multidi- mensional saddle-focus type, and spiral chaos *Mathematics of the USSR-Sbornik* **73** 415–43 http://stacks.iop.org/0025-5734/73/i=2/a=A07
[47] Eckhardt B and Mersmann A 1999 Transition to turbulence in a shear flow *Phys. Rev.* E **60** 509–17
[48] Herde D, Thiele U, Herminghaus S and Brinkmann M 2012 Driven large contact angle droplets on chemically heterogeneous substrates *Europhys. Lett.* **100** 16002
[49] Varagnolo S, Ferraro D, Fantinel P, Pierno M, Mistura G, Amati G, Biferale L and Sbragaglia M 2013 Stick-slip sliding of water drops on chemically heterogeneous surfaces *Phys. Rev. Lett.* **111** 066101
[50] Thiele U 2011 On the depinning of a drop of partially wetting liquid on a rotating cylinder *J. Fluid Mech.* **671** 121–36
[51] Pailha M, Hazel A, Glendinning P and Juel A 2012 Oscillatory bubbles induced by geometrical constraint *Phys. Fluids* **24** 021702
[52] Thompson A B, Juel A and Hazel A L 2014 Multiple finger propagation modes in hele-shaw channels of variable depth *J. Fluid Mech.* **746** 123–64
[53] Pototsky A, Archer A J, Savel'ev S E, Thiele U and Marchesoni F 2011 Ratcheting of driven attracting colloidal particles: temporal density oscillations and current multiplicity *Phys. Rev.* E **83** 061401
[54] Hashish M 1988 Visualization of the abrasive-waterjet cutting proces *Exp. Mech.* **28** 159–69
[55] Folkes J 2009 Waterjet - an innovative tool for manufacturing *J. Mater. Process. Technol.* **209** 6181–9

[56] Friedrich R, Radons G, Ditzinger T and Henning A 2000 Ripple formation through an interface instability from moving growth and erosion sources *Phys. Rev. Lett.* **85** 4884–7
[57] Radons G, Ditzinger T, Friedrich R, Henning A, Kouzmichev A and Westkämper E 2005 Nonlinear dynamics and control of ripple formation in abrasive water-jet cutting *Nonlinear Dynamics of Production Systems* (Weinheim: Wiley-VCH Verlag) pp 391–410
[58] Beltrame P, Hänggi P and Thiele U 2009 Depinning of three-dimensional drops from wettability defects *Europhys. Lett.* **86** 24006
[59] Tseluiko D, Galvagno M and Thiele U 2014 Collapsed heteroclinic snaking near a heteroclinic chain in dragged meniscus problems *Eur. Phys. J.* E **37** 33
[60] Siggers J H 2003 Dynamics of target patterns in low-Prandtl-number convection *J. Fluid Mech.* **475** 357–75
[61] Krauskopf B and Oldeman B E 2004 A planar model system for the saddle-node Hopf bifurcation with global reinjection *Nonlinearity* **17** 1119–51